How to cite: *Angew. Chem. Int. Ed.* **2026**, e22380
doi.org/10.1002/anie.202522380

Non-aqueous Hydrogen Oxidation | ***Very Important Paper***

Surface Modulated Platinum Electrocatalyst via Single Atom Nickel Promoter for Durable Non-aqueous Hydrogen Oxidation

Kuiquan Yan, Yang Hong, Zhi Wang, Depeng Wang, Tong Liu, Haixia Zhong, and Xinbo Zhang**

Abstract: Electrocatalytic hydrogen oxidation reaction (HOR) plays crucial role in various renewable energy conversion processes. Particularly, it offers new opportunities for sustained electrochemical ammonia synthesis when coupled with lithium-mediated nitrogen reduction. But it remains tremendous challenges due to slow reaction kinetics and rapid poisoning of catalysts in non-aqueous electrolyte. Here, we report Ni single atom mediated Pt sites on Ni substrate ($PtNi_1$/Ni) to boost efficient and durable HOR in organic electrolyte. $PtNi_1$/Ni exhibits high performance of nearly 100% Faradaic efficiency (FE) and long-term stability over 1000 h in tetrahydrofuran (THF) electrolyte, far beyond commercial Pt electrode (<0.2 h). Theoretical calculations combined with spectroscopic characterizations indicated that Ni single atom contributes to tailoring electronic structure of Pt sites via ligand effects, which effectively reduces the energy barrier of the rate-determining step, and simultaneously as synergistic site in suppressing organic poison species through changing THF adsorption configuration and increasing energy barriers of THF oxidative decomposition. In the lithium-mediated electrochemical ammonia synthesis electrolyzer, it also exhibits good feasibility with high ammonia FE of ~62%. This work sheds light on the effective strategy of single atom doping for developing active and durable nonaqueous HOR electrocatalyst and presents insightful understanding of anti-poisoning mechanism.

Introduction

Ambient ammonia synthesis via lithium-mediated nitrogen reduction emerges as one promising distributed production system,[1] which can overcome the challenges of harsh operated conditions (high-temperature and pressure) and large amount of CO_2 emissions in traditional energy-intensive Haber–Bosch process. In many cases, the proton resource derives from oxidation of organic solvents, such as tetrahydrofuran (THF), however, which inevitably result in poor stability of the system and thus hinder continuous ammonia synthesis. Recently, progress of the continuous proton supply via hydrogen oxidation reaction (HOR) instead of sacrificing organic solvent offers new opportunities for the sustainable ammonia synthesis in a flow system.[2] Unfortunately, in contrast to the well-established rational design principles of HOR electrocatalysts[3–9] in aqueous electrolytes[10–15] and the comprehensive understanding of reaction mechanisms, the electrocatalytic HOR in organic electrolyte remains less clear. Beside with the intrinsically slow reaction kinetics, one daunting challenge lies on the rapid deactivation of catalytic sites for non-aqueous HOR, typically within minutes, due to the irreversible surface poisoning by solvents or carbon-based intermediates.[16] Therefore, rational design of electrocatalyst with high activity and strong resistance to organic poison species is critical for HOR in organic electrolyte toward the sustainable ammonia synthesis.

Metal doping engineering has been well explored in building stable and efficient electrocatalytic interfaces.[17] For example, decorating Pt surfaces with dopants (Ni, In, Ru, Rh, and Ir) effectively adjusted the interfacial environment to enhance the alkaline HOR activity.[18–22] Besides, incorporating oxyphilic atoms like Mo was powerful to optimize the adsorption of H and CO intermediate and thus boost anti-CO-poisoning hydrogen oxidation in alkaline media.[23] However, there is still a high risk of unexpectedly generating second inferior phase and blocking active sites through the doping modification. Moreover, it also fails in selectively enhancing the interaction of hydrogen related intermediates while simultaneously suppressing the adsorption of poisonous organic species in non-aqueous electrolyte through simply modulating the electronic structure of Pt sites. Inspired by the

[*] K. Yan, Y. Hong, Z. Wang, D. Wang, Prof. T. Liu, Prof. H. Zhong, Prof. X. Zhang
State Key Laboratory of Rare Earth Resource Utilization, Changchun Institute of Applied Chemistry, Chinese Academy of Sciences, No. 5625, Renmin Street, Chaoyang District, Changchun 130022, P.R. China
E-mail: hxzhong@ciac.ac.cn
xbzhang@ciac.ac.cn

K. Yan, Y. Hong, Z. Wang, D. Wang, Prof. T. Liu, Prof. H. Zhong, Prof. X. Zhang
School of Applied Chemistry and Engineering, University of Science and Technology of China, No.96, Jinzhai Road, Baohe District, Hefei, Anhui 230026, P.R. China

Prof. T. Liu, Prof. H. Zhong, Prof. X. Zhang
China-Belarus Belt and Road Joint Laboratory on Advanced Materials and Manufacturing, Changchun Institute of Applied Chemistry, Chinese Academy of Sciences, No. 5625, Renmin Street, Chaoyang District, Changchun 130022, P.R. China

Additional supporting information can be found online in the Supporting Information section

promise of high atom utilization in single metal atom catalysts, single metal atom doping route is expected in maximizing the activation of Pt atoms nearby dopants with minimal site blockage. This foreign doping single metal atom acts a ligand for finely optimizing the coordination and electronic structure of adjacent Pt centers and a cocatalyst to synergistically balance the adsorption for hydrogen-based intermediates and organic species. Despite with grand challenges, the research for regulated Pt catalysts through single atom doping is of paramount need for the active and stable HOR.

Here, we introduce the surface modified Pt nanoparticles ($PtNi_1$) on Ni substrates as the active and stable all-in-one electrode for electrocatalytic HOR in organic electrolyte through Ni single atom doping engineering, in which single atom Ni was employed to optimize the adsorption/desorption ability of hydrogen-related intermediates and induce synergism between Pt and Ni sites for suppressing THF adsorption and oxidation. Note that no Ni aggregation and second Ni-based phase were found. As expected, $PtNi_1$ electrocatalyst boosts an efficient and durable HOR process, along with high HOR Faradaic efficiency (FE, ~100%) and high stability over 1000 h in THF electrolyte, largely outperforming the commercial Pt electrode (less than 0.2 h). We also demonstrate its practical utility by coupling with lithium-mediated nitrogen reduction for continuous ammonia synthesis under ambient conditions, achieving ammonia FE of ~62% at −4 mA cm^{-2} for more than 80 h and the reduced energy consumption of ~42% compared to single batch reactor with solvent oxidation based on the simple technical and economic analysis. Through the in situ characterization and theoretical calculations, we found that Ni atom doping optimizes nearby Pt sites, which effectively promote the HOR by the favorable hydrogen activation and reducing the energy barriers of *H formation and desorption. Additionally, this Ni promoter contributes to suppressing the poison of Pt site through the strong adsorption of THF molecules with changed configuration and higher energy barrier of THF oxidation on either Ni or Pt site of $PtNi_1$ compared to pure Pt electrode. Our work verifies the crucial role of single atom doping strategy in developing advanced Pt-based electrocatalyst for non-aqueous HOR with high activity, high resistance to organic species and long-term durability, and unveils deep insights on the anti-poisoning mechanism in organic electrolyte systems.

Results and Discussion

Synthesis and Characterization

The self-supported electrode (Ni foil) loaded with $PtNi_1$ nanoparticles (NPs) was prepared through a facile chemical deposition process ($PtNi_1$/Ni, Figure S1).[24] As indicated by X-ray diffraction (XRD) analysis of $PtNi_1$ powder (Figure S2), three dominant diffraction peaks correspond to (111), (200), and (220) crystallographic planes of the face-centered cubic (fcc) structure of Pt, respectively, excluding the formation of second Ni-based phase. Inductively coupled plasma-atomic emission spectrometry (ICP-AES, Table S1) of collected particles confirmed the presence of Ni (1.6 at%). Scanning electron microscopy (SEM) characterization (Figure S3) revealed that $PtNi_1$ catalyst is composed of tightly packed nanoparticles. It is worth noting that $PtNi_1$ particles were successfully deposited on nickel foam as well ($PtNi_1$/NF, Figures S4 and S5), which can directly act as the integrated gas diffusion electrode in the flow cell system. Aberration-corrected high-angle annular dark-field scanning transmission electron microscopy (AC-HAADF-STEM) images (Figure 1a) further revealed the nanoscale structure with a narrow size distribution of several nanometers (Figure 1d), while selected area electron diffraction (SAED) analysis (inset in Figure 1a) confirmed the polycrystalline structure with characteristic halation rings corresponding to (111), (200), and (220) planes.[25] As shown in the distinct Z-contrast difference in the AC-HAADF-STEM images and their three-dimensional (3D) fitting maps (Figure 1b), darker spots indicative of Ni atoms were embedded within the brighter Pt matrix. It is thus clear that Ni dopants are atomically dispersed within Pt lattice. This arrangement is further validated by the intensity profiles along lines a–c (Figure 1c,e) and energy-dispersive X-ray spectroscopy (EDS) elemental mapping (Figure 1f), which shows a homogeneous distribution of Ni atoms on Pt NPs surface. Additionally, an EDS line scan across $PtNi_1$ nanoparticle (Figure 1f,g) further illustrates the well dispersion of the doped Ni atoms within Pt lattice.

X-ray photoelectron spectroscopy (XPS) was then employed to elucidate the electronic structures of this catalyst. Pt *4f* peaks emerged at approximately 70.5 and 74.5 eV and Ni *2p* peaks were observed at approximately 855.0 and 873.0 eV (Figure S6),[26] which verify that majority of surface Pt was in the metallic state while surface Ni was slightly oxidized. Notably, a negative shift of 0.3 eV in Pt *4f* peak toward lower binding energy was observed for $PtNi_1$ compared to metallic Pt (Figure S6a). Conversely, Ni *2p* peak exhibited about 0.15 eV positive shift toward higher binding energy compared to metallic Ni (Figure S6b). This is likely due to the electron transfer from Ni to Pt with higher electronegativity.[26] The valence states of Pt and Ni were further investigated by the Pt L_3-edge and Ni K-edge X-ray absorption near-edge structure (XANES) spectra[27] (Figure 1h,j). Taking Pt foil and PtO_2 as references, Pt valence state in $PtNi_1$ was close to 0 (Figure 1h,i). Ni species of $PtNi_1$ was slightly oxidized with valence state of around + 0.78, which is between Ni (0) foil and NiO (+2) reference sample (Figure 1j–k). The extended X-ray absorption fine structure (EXAFS) analysis further corroborated the interaction between Pt and Ni species. The dominant peak at 2.45 Å was ascribed to Pt-Pt of $PtNi_1$ catalysts (Figure S7a), which is slightly lower than that observed in bulk Pt (2.51 Å). The characteristic Ni-Ni signal was observed at 2.16 Å for Ni foil and NiO reference sample presents the interaction signals of Ni–O and Ni–O–Ni at 1.63 and 2.72 Å, respectively (Figure S7b). Differently, Ni K-edge EXAFS spectrum of $PtNi_1$ exhibited a dominant scattering peak at 1.71 Å, which was likely due to Ni–O bond,[28] verifying the doping single Ni atom within the Pt particles and excluding the generation of metallic Ni phase. These results were also confirmed by the wavelet transform EXAFS analysis (Figure S8). Combined

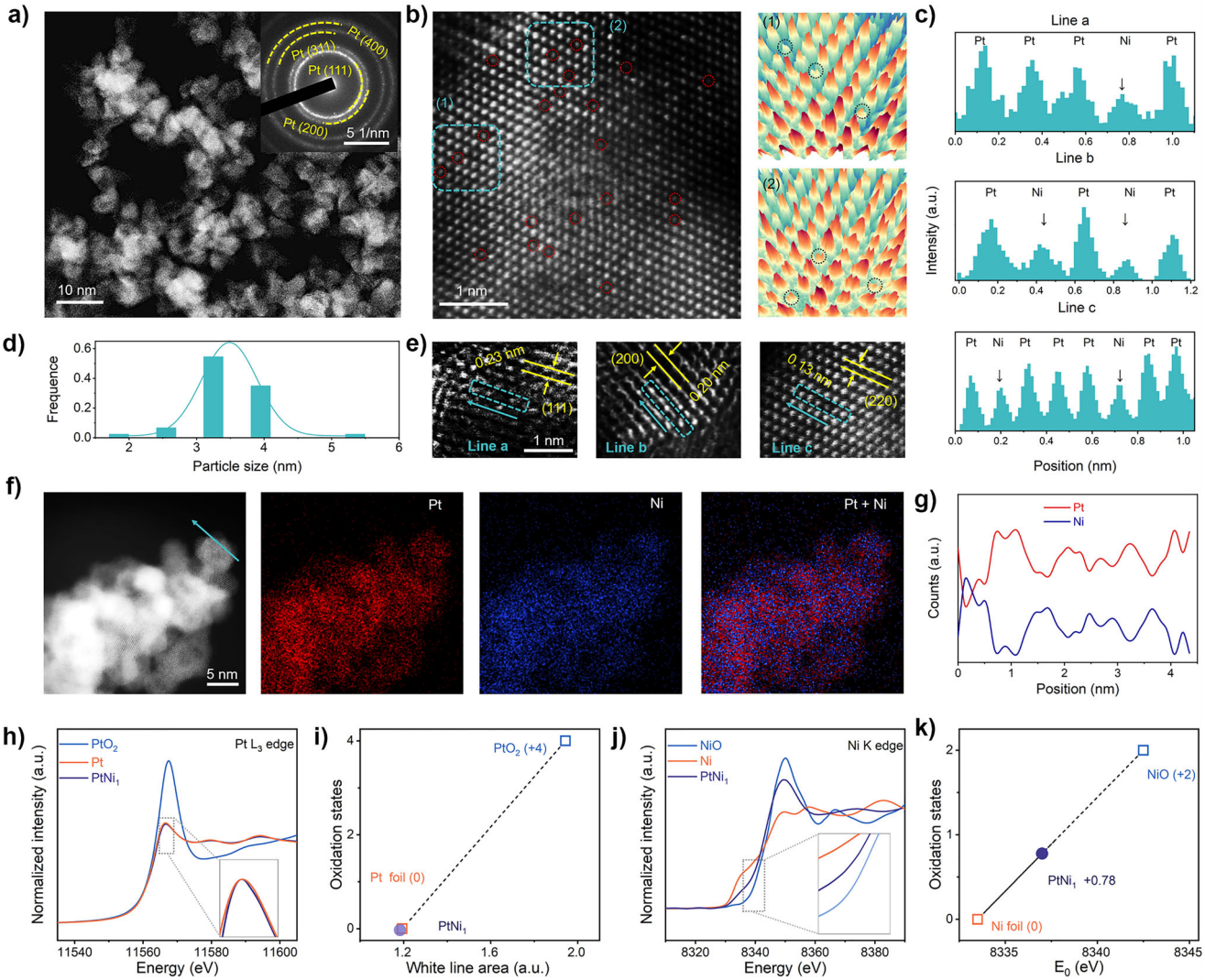

Figure 1. Morphology and structure characterizations of $PtNi_1$ catalyst. a) AC-HAADF-STEM image of $PtNi_1$ catalyst. Inset: SAED pattern. b) High-resolution AC-HAADF-STEM image of $PtNi_1$ catalyst and the accordingly selected 3D atom-overlapping mapping. c) Line-scanning intensity profiles along lines a–c in the image from (e); d) particle size distribution of $PtNi_1$ nanoparticles. e) Atomically resolved HAADF-STEM images of $PtNi_1$ catalyst. f) AC-HAADF-STEM image of $PtNi_1$ catalyst and its corresponding EDS elemental mapping. g) EDS line scan profiles for Pt (red) and Ni (blue) traversing the region marked by the arrow in the image f). h) Pt L_3-edge XANES spectra for Pt foil, PtO_2 and $PtNi_1$ catalyst. j) Ni K-edge XANES spectra for Ni foil, NiO, and $PtNi_1$ catalyst. i, k) Valence state analysis of Pt and Ni in $PtNi_1$ catalyst.

with AC-HAADF-STEM images, it was confirmed that single-atom Ni doped Pt nanoparticles ($PtNi_1$) on Ni foil as the all-in-one electrode was successfully synthesized.

Electrocatalytic HOR Performance

First, the electrochemical HOR performance of $PtNi_1$/Ni foil electrode was evaluated in a one-compartment cell using 1 M $LiBF_4$ in THF with 0.25 vol.% EtOH as electrolyte under argon atmosphere glove box. As shown in Figures 2a and S9, $PtNi_1$/Ni exhibits no oxidation peak at 0.6 V versus Pt pseudo reference electrode under Ar-saturated electrolyte while a more intense oxidation peak in cyclic voltammetry (CV) curves under H_2 bubbled electrolyte compared to Pt electrode, demonstrating superior catalytic activity compared to Pt. Additionally, the observed diffusion-limited current density of 5.1 mA cm^{-2} at high operated potential of 0.7 V versus Pt is attributed to the mass transfer limitations related to H_2 oxidation on $PtNi_1$/Ni, which is larger than Pt electrode (2.6 mA cm^{-2}), highlighting the significant role of Ni dopant in promoting HOR. Consistent with previous findings,[29] during chronopotentiometry (CP) testing with constant current density of 2 mA cm^{-2}, Pt electrode exhibited a rapid deactivation, along with the increasing anode potential even up to 1.4 V versus Pt (Figure 2b), where THF oxidation occurs[2] (Figure 2c). In stark contrast, $PtNi_1$/Ni maintained the stable HOR with low potential (~0.3 V versus Pt) at 2 mA cm^{-2} (Figure 2b). Besdies, $PtNi_1$/Ni also presented low Tafel slope (54.4 mV dec^{-1}) and thus faster HOR kinetics in comparison with Pt electrode (179.4 mV dec^{-1}, Figure S10). Thus, upon single atom Ni doping, $PtNi_1$/Ni demonstrated the

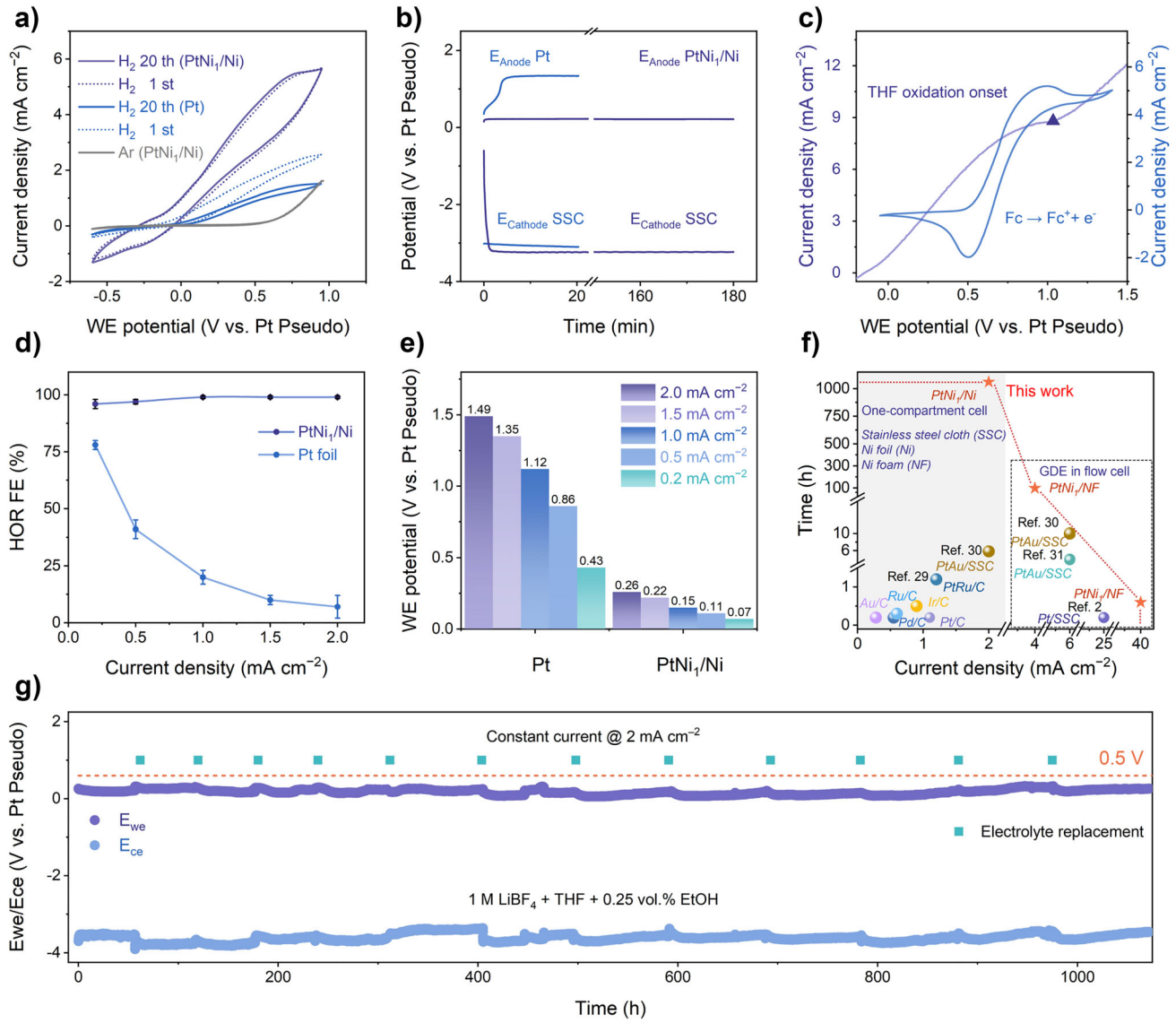

Figure 2. Electrocatalytic HOR performance. a) CV curves of $PtNi_1/Ni$ and Pt electrodes in 1 M $LiBF_4$/THF containing 0.25 vol.% EtOH (THF electrolyte) saturated with H_2 or Ar. WE: working electrode. b) Chronopotentiometry (CP) curves of Pt and $PtNi_1/Ni$ in a one-compartment cell with THF electrolyte, using H_2 at 2 mA cm^{-2}. c) Linear sweep voltammogram obtained in THF electrolyte with H_2 saturation and CV curves in THF electrolyte containing 250 mM ferrocene. d) Selectivity comparison of HOR between $PtNi_1/Ni$ and Pt electrode at different current densities. e) Anode potential for $PtNi_1/Ni$ and Pt foil at various current densities (0.2, 0.5, 1.0, 1.5, and 2 mA cm^{-2}). f) Stability comparison with other reported catalysts.[2,29–31] g) Long-term stability test using $PtNi_1/Ni$ as the anode.

apparent enhancement in stability and catalytic activity for HOR compared to Pt electrode.

Faradaic efficiency for hydrogen oxidation was indirectly quantified by monitoring the concurrent ferrocene oxidation reaction[2] (details shown in supporting information, Figures 2d and S11). This is according to that ferrocene is thermodynamically more challenging to be oxidized than H_2 but easier than THF (Figure 2c), the applied current is expected to first oxidize H_2 to the solvated protons, which is assumed as the kinetically favorable HOR process, followed by the ferrocene oxidation to ferrocenium once HOR becomes diffusion limited. Therefore, control experiments were also carried out where no current was applied, in which background ferrocenium levels were quantified (Figure S11). $PtNi_1/Ni$ shows high HOR selectivity with near-unity HOR FE (close to 100%) at applied current densities from 0.2 to 2 mA cm^{-2} (Figure 2d). Figure 2e exhibits the anode potential at different current densities. Unfortunately, Pt electrode presents the potential of 1.12 and 1.49 V versus Pt at 1 and 2 mA cm^{-2}, respectively, where THF oxidation occurs, resulting in the fast deactivation of Pt for HOR. $PtNi_1/Ni$ responses quickly to the changing current density and delivers only 0.26 V versus Pt at 2 mA cm^{-2}. The observed reduction in anode potential of $PtNi_1/Ni$ verifies the superiority over Pt in improving the overall energy efficiency by coupling the selective HOR.[30]

Moreover, for the practical application, we conducted HOR tests under harsh conditions (Figure 2g). Impressively, $PtNi_1$/Ni exhibited exceptional electrolysis stability over 1000 h, with almost no noticeable decay in activity, which is largely better than the reported catalysts. (Figure 2f)[2,29–31] EXAFS and AC-HAADF-STEM characterizations of $PtNi_1$ after CP test revealed no apparent agglomeration, leaching, or morphological degradation of Ni single atom, confirming its long-lastingly stable structure during HOR (Figures S2, S7, and S12 and S13). This long-term stability strongly suggests its potential for the implementation in continuous ammonia synthesis processes.

Continuous Ammonia Electrosynthesis Device Performance

In order to evaluate the application of $PtNi_1$ catalyst in ammonia synthesis via Li-mediated nitrogen reduction (Li-NRR), we studied the coupled HOR/Li-NRR process (Figure 3a). The performance of synthetic ammonia was investigated in THF and dimethyl diglycol (DG) solvent system (Figure 3b–e), which been used as suitable solvents for ammonia synthesis.[32] To enable continuous ammonia synthesis at high current density, $PtNi_1$ on Ni foam ($PtNi_1$/NF) was directly utilized as an gas diffusion anode in flow cell, which affords a higher electrochemically active surface area (Figure S14) to expose rich active sites and sufficient mass transfer, as well as high selectivity for HOR (Figure S15).

To mitigate excessive lithium deposition and enhance synthesis efficiency, a cyclic potential strategy was employed during electrochemical testing.[33] The ammonia FE for Li NRR was determined to be $60.9 \pm 1\%$ in THF and $62.3 \pm 2\%$ in DG in flow cell (Figures 3b and S16–S20). Long-term stability tests were further conducted in a continuous-flow reactor. $PtNi_1$/NF evidenced its operational stability across different solvents with no apparent increase of anode potential (Figure 3e). Throughout the extended operation, the anode potential remained below 1 V, contributing to sustainable hydrogen supply. The NMR analysis of the electrolyte before and after the electrolysis suggests no apparent solvent oxidation occurs in these systems (Figure S21). In the DG solvent system, an ammonia FE of ~62% and the yield rate ~0.78 nmol s^{-1} cm^{-2} was achieved over 80 h of operation (Figure 3c,d), with only slight degradation observed towards the end. The THF system maintained 60% FE and 4.51 nmol s^{-1} cm^{-2} yield rate after 10 h. These results highlight the promising operational stability and versatility of $PtNi_1$/NF across different solvent systems. When the operational current density was increased from − 4 to −40 mA cm^{-2} in DG electrolyte (Figures 3f and S22 and S23), this system also maintained the efficient ammonia generation with ammonia FE of 56.6% and yield rate of 7.77 nmol s^{-1} cm^{-2}. In addition, we also demonstrated the feasibility of electrochemical ammonia synthesis in a dimethyl ether (DME)-based electrolyte system (Figures S24 and S25). Note that, the gaseous ammonia is easily collected as NH_4Cl powder (Figure S26), which further highlights the advantage of the continuous flow cell in improving the efficiency of ammonia generation.

Technical and economic analysis was further conducted based on the process models developed by Ruud kortlever team.[34] As shown in Figure 3g, under these operating conditions, the average anode potential was maintained at approximately 0.8 V versus a Pt reference electrode, resulting in an overall cell voltage of 4.2 V in the flow cell system. However, in the single cell test, the cell voltage increased as high as 7.6 V, which is likely associated with the high overpotential of solvent oxidation of the anode for hydrogen supply. The energy consumption of electrolyzer is estimated to be around 114.81 $GJt^{-1}{}_{NH3}$ based on $PtNi_1$ system, which is less than that of the single batch reactor (198.59 $GJt^{-1}{}_{NH3}$, Figure 3h).[35] According to the extended energy consumption analysis (Figures S27–S29) of the entire process chain, including raw material processing, ammonia separation, and material recycling upon ideal systems, it was demonstrated that the integration of hydrogen oxidation confers dual advantages: i) directly decreasing the anode potential for lowering the overall energy consumption of the electrolysis unit; ii) optimizing downstream separation and purification process of ammonia and air separation units, along with a significant reduce in energy input. Therefore, when coupling with anodic HOR using $PtNi_1$, energy efficiency for Li NRR for ammonia synthesis can be effectively enhanced.

HOR Mechanism Exploration

Infrared spectroscopy was further applied to monitor electrolyte evolution during reaction process at a constant current density of 2 mA cm^{-2}. The initial spectrum of the electrolyte (0 min) displayed the characteristic vibrations of THF at 1070 cm^{-1} (C–O–C stretch), 912 cm^{-1} (ring deformation) and 659 cm^{-1} (ring breathing), with an additional fingerprint at 1460 cm^{-1} (Figure 4a–c).[36,37] Notably, progressive attenuation of C–O–C (1070 cm^{-1}) and ring breathing (659 cm^{-1}) signals after 60 min was observed in the Pt electrode system, concomitant with emerging new peaks at 1172 cm^{-1} (aryl–O stretch) and 991 cm^{-1} (alkyl–O stretch). The appearance of typical furan signatures (~869 and 1460 cm^{-1}) within 60 min of operation (Figure 4a,b, white line) indicated THF oxidation at Pt electrode, which was consistent with electrochemical results (Figure 2b). THF oxidation into furan formation on Pt electrode after 5 h operation was also identified by the ^1H NMR spectra in Figure S30a. In contrast, the electrolyte remained its chemical structure when using $PtNi_1$/Ni electrode (Figure S30b). Figure 4c also displays that stable THF spectra was monitored throughout operation (Figure 4c) on $PtNi_1$/Ni, with no detectable signals from oxidation products or NMR-detectable byproducts. Consistent spectral evolution was observed at the electrode-electrolyte interface (Figure S31). These results claim that both active-site poisoning and electrolyte decomposition are inhibited on $PtNi_1$/Ni compared to Pt electrode.

Density functional theory (DFT) calculations were then used to elucidate the role of Ni single atoms in modulating Pt sites toward HOR. Based on structural characterizations, Pt (111) model was built to investigate the oxidation of THF and hydrogen for Pt and Ni single atom doping Pt catalysts

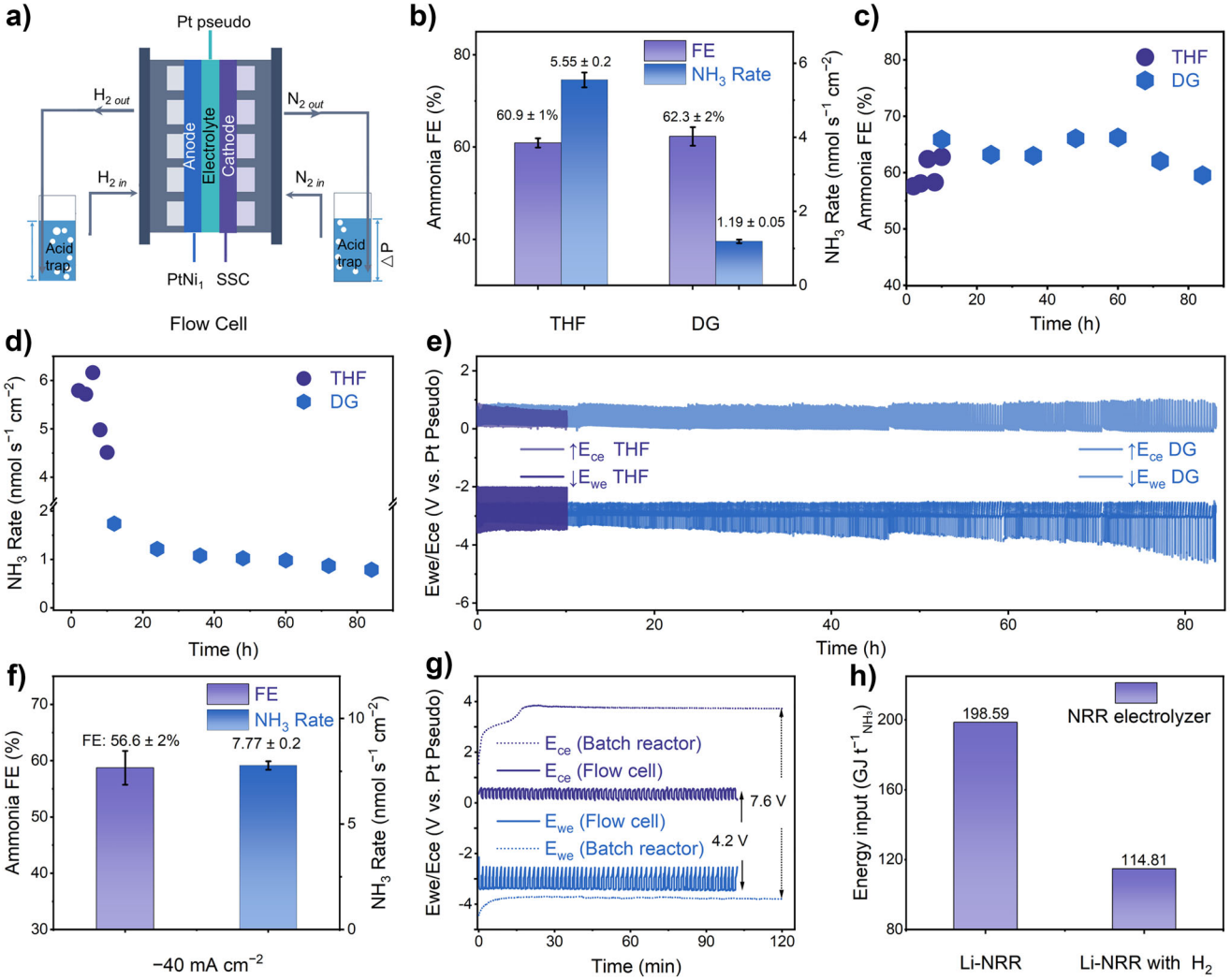

Figure 3. Ammonia electrosynthesis in the assembled continuous-flow reactor. a) Schematic diagram and configuration of the continuous-flow reactor. b) Ammonia FE, yield rate at −4 mA cm^{-2} in THF and DG electrolyte c) FE and d) yield rate of ammonia at −4 mA cm^{-2} during the long-term test. e) Long-term stability of Li-NRR process in a continuous-flow reactor. f) FE and yield rate of ammonia at −40 mA cm^{-2} in DG electrolyte. g) Chronopotentiometry curves in single batch reactor and the flow cell. h) Energy input of NRR electrolyzer with different processes. Additional energy input for H_2 production via water electrolysis is not included for NRR electrolyzers.

(Figure S32). Projected density of states (PDOS) analysis (Figure 4d) reveals that the overall electronic structure of Pt is not changed significantly upon trace Ni single atom doping. While Pt d-orbital features near the Fermi level (Figure S33) are adjusted. Incorporation of trace Ni into Pt lattice results in the downshift of the d-band center (from − 2.38 to − 2.76 eV) of Pt sites, which will reduce the overlap between d-orbitals of Pt and adsorbate antibonding orbitals and thereby weaken the adsorption energy.[38,39] Indeed, as shown in Figure 4e, the adsorption of hydrogen is slightly weaker on Pt site of $PtNi_1$ with adsorption energy of − 0.94 eV than that of Pt (−1.06 eV), which is favorable for effective H_2 dissociation. Furthermore, the HOR process was studied. Kinetic analysis reveals that hydrogen desorption (Volmer step) is the rate-determining steps (Figures 4f and S34). Pure Pt requires higher energy barriers of 0.51 eV for *H desorption. After introduction of Ni single atoms, Pt sites nearby Ni atom could facilitate hydrogen desorption with lower energy barrier of 0.36 eV, significantly enhancing HOR kinetics.

According to IR and NMR results, the side reaction of THF oxidation was further investigated on Pt and $PtNi_1$. Bader charge analysis discloses the electron transfer from Ni to Pt, with Ni oxidation states near + 1.83 |e|, aligning with XAFS and XPS results. The positive charge accumulation around Ni atoms (Figure S35), which enhances the local THF adsorption through strong Ni–O interactions with electronegative oxygen (Figure 4g). THF adsorption configurations (planar/vertical) and energetics (ΔG_{THF*}) at stable sites near Ni dopants in $PtNi_1$ versus pure Pt were then discussed (Figure S36). Notably, THF adsorption on Pt sites of $PtNi_1$ is moderate with ΔG_{THF*} of –0.89 eV via vertical adsorption and –0.54 eV via planar model (Figure S36c,d), which are both substantially weaker than that of Ni sites (–0.96 and –0.59 eV), respectively. This energy difference implies the preferential

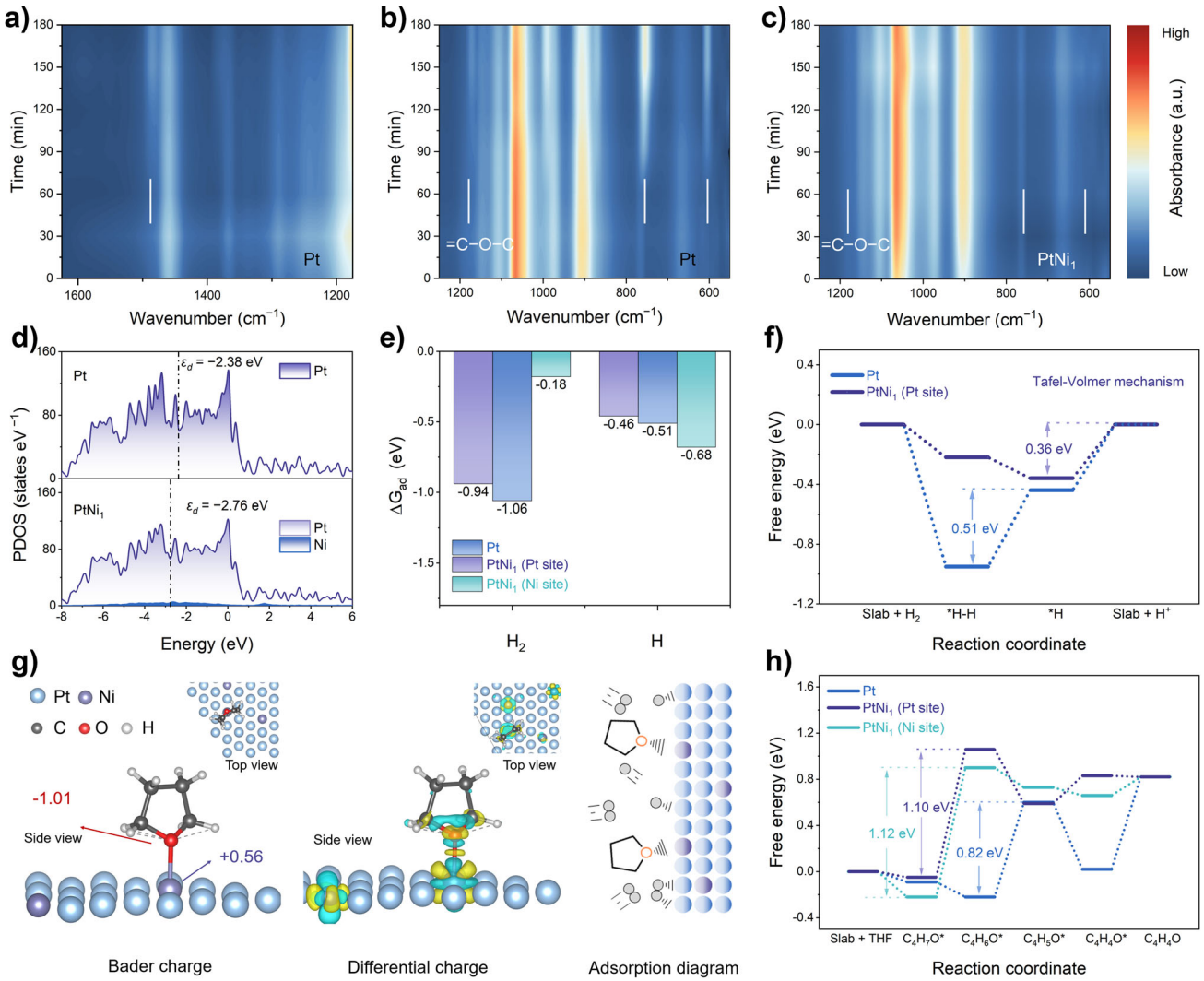

Figure 4. Mechanism study. a) and b) IR spectra of electrolyte during HOR over Pt foil under reaction conditions c) IR spectra of electrolyte using $PtNi_1$/Ni catalyst under the same conditions. d) Calculated PDOS of Pt and $PtNi_1$. e) Adsorption energy of hydrogen and the related intermediates for $PtNi_1$ and pure Pt. f) Gibbs free energy diagram of HOR for Pt and $PtNi_1$. g) Bader charge and differential charge density analyses for $PtNi_1$ after THF adsorption and the schematic adsorption diagram. h) Gibbs free energy diagram of THF oxidation reaction for Pt and $PtNi_1$.

vertical THF adsorption on Ni centers. Accordingly, the adsorption diagram through vertical model was proposed (Figure 4g) for $PtNi_1$. As for pure Pt, planar adsorption is more favorable (Figure S36d) due to higher adsorption energy of –1.2 eV. This is also higher than the adsorption energy of hydrogen on Pt (–1.07), which suggests the possible blockage of the active sites for HOR. Through Ni single atom doping, the adsorption of hydrogen intermediates and the poison intermediates are balanced in $PtNi_1$ catalysts. By localizing THF at Ni sites, the possible dense organic passivation layer that would block Pt active sites is disrupted. Thus, reaction process of THF oxidation was further studied (Figures 4h and S37–S40). The calculated energy barrier for RDS of THF oxidation (Figure 4h) on Ni (1.12 eV) and Pt sites (1.10 eV) for $PtNi_1$ site are both higher than that for pure Pt (0.82 eV), indicating effective suppression of THF decomposition on $PtNi_1$.

Conclusion

In conclusion, surface regulated Pt catalyst was developed for non-aqueous HOR through Ni single atom doping engineering without blocking the active phase. Here, Ni single atom acts as modulator to optimize the local environment and electronic states of adjacent Pt atoms for improving the activity, and simultaneously services as synergistic site for breaking the organic passivation layer and addressing the poisoning problem. The optimized $PtNi_1$ catalyst demonstrated high selectivity and prolonged operation (>1000 h) with negligible performance degradation under the applied current density. We also verified its feasibility in the continuous ammonia synthesis when coupled with Li-NRR, realizing high ammonia selectivity more than 60%. This single atom doping engineering represents a versatile and broadly applicable strategy for tailoring the catalytic properties of precious metal

nanomaterials, which is expected to be applicable when using other dopant elements such as Fe, Co, or Cu species and catalytic reactions.

Supporting Information

Supplemental information can be found in *Supporting information.docx*. Additional experimental details, materials, and methods, including XRD patterns, SEM, TEM, AC-HAADF-STEM images, IR, ^{1}H NMR and XPS spectra, EXAFS analysis, electrochemical data (CV, ECSA, CP) for $PtNi_1$ catalysts, supplementary tables and DFT models (Supplemental experimental procedures, Figures S1–S40 and Tables S1–S6).

Acknowledgements

This work was supported by the National Key R&D Program of China (2021YFB4000401), the National Natural Science Foundation of China (52273277, U24A2062), Jilin Province Science and Technology Development Plan Funding Project (SKL202302039), and Youth Innovation Promotion Association CAS (2021223). These authors thank the staff of beamline BL13SSW at Shanghai Synchrotron Radiation Facility for XAFS experiment support. The authors also thank Dr. L. Li from Electron Microscopy Center of Jilin University for TEM measurement and analysis. Zhong acknowledges funding from the National Natural Science Foundation of China Outstanding Youth Science Foundation of China (Overseas).

Conflict of Interests

The authors declare no conflict of interest.

Data Availability Statement

The data that support the findings of this study are available from the corresponding author upon reasonable request.

Keywords: All-in-one electrode · Lithium-mediated ammonia synthesis · Non-aqueous hydrogen oxidation reaction · Platinum electrocatalyst · Single atom modulator

[1] S. J. K. Forrest, B. Schluschaß, E. Y. Yuzik-Klimova, S. Schneider, *Chem. Rev.* **2021**, *121*, 6522–6587, https://doi.org/10.1021/acs.chemrev.0c00958.
[2] N. Lazouski, M. Chung, K. Williams, M. L. Gala, K. Manthiram, *Nat. Catal.* **2020**, *3*, 463–469, https://doi.org/10.1038/s41929-020-0455-8.
[3] C. Xia, F.-M. Li, C. He, S. Zaman, W. Guo, B. Y. Xia, *Fundam. Res.* **2025**, *5*, 2537–2552, https://doi.org/10.1016/j.fmre.2024.04.017.
[4] T. Yang, X. Yang, N. Gao, M. Tang, X. Wang, C. Liu, W. Xing, J. Ge, *eScience* **2024**, *4*, 100230, https://doi.org/10.1016/j.esci.2024.100230.
[5] P. Li, J. Zhong, Y. Fu, Z. Du, L. Jiang, Y. Han, J. Luxa, B. Wu, Z. Sofer, Q. Wei, W. Yang, *Energy Environ. Mater.* **2024**, *7*, e12716, https://doi.org/10.1002/eem2.12716.
[6] L. An, T. Zhao, W. Lei, C. Yang, J. Yang, D. Wang, *eScience* **2025**, *5*, 100400, https://doi.org/10.1016/j.esci.2025.100400.
[7] R. Li, D. Wu, P. Rao, P. Deng, J. Li, J. Luo, W. Huang, Q. Chen, Z. Kang, Y. Shen, X. Tian, *Carbon Energy* **2023**, *5*, e294, https://doi.org/10.1002/cey2.294.
[8] H.-R. Pan, T. Tang, J.-S. Hu, *Fundam. Res.* **2021**, *1*, 461–465, https://doi.org/10.1016/j.fmre.2021.06.008.
[9] S. S. Hardisty, X. Lin, A. R. J. Kucernak, D. Zitoun, *Carbon Energy* **2024**, *6*, e409, https://doi.org/10.1002/cey2.409.
[10] Y. Hu, T. Chao, Y. Dou, Y. Xiong, X. Liu, D. Wang, *Adv. Mater.* **2025**, *37*, 2418504, https://doi.org/10.1002/adma.202418504.
[11] W. Li, D. Wang, Y. Zhang, L. Tao, T. Wang, Y. Zou, Y. Wang, R. Chen, S. Wang, *Adv. Mater.* **2020**, *32*, 1907879, https://doi.org/10.1002/adma.201907879.
[12] L. Su, H. Wu, S. Zhang, C. Cui, S. Zhou, H. Pang, *Adv. Mater.* **2025**, *37*, 2414628, https://doi.org/10.1002/adma.202414628.
[13] Y. Yang, C. R. Peltier, R. Zeng, R. Schimmenti, Q. Li, X. Huang, Z. Yan, G. Potsi, R. Selhorst, X. Lu, W. Xu, M. Tader, A. V. Soudackov, H. Zhang, M. Krumov, E. Murray, P. Xu, J. Hitt, L. Xu, H.-Y. Ko, B. G. Ernst, C. Bundschu, A. Luo, D. Markovich, M. Hu, C. He, H. Wang, J. Fang, R. A. DiStasio, L. F. Kourkoutis, et al., *Chem. Rev.* **2022**, *122*, 6117–6321, https://doi.org/10.1021/acs.chemrev.1c00331.
[14] E. Antolini, *Energy Environ. Sci.* **2009**, *2*, 915–931, https://doi.org/10.1039/b820837a.
[15] X. Zhang, X. Xiao, J. Chen, Y. Liu, H. Pan, W. Sun, M. Gao, *Energy Environ. Sci.* **2022**, *15*, 4511–4526, https://doi.org/10.1039/D2EE02216H.
[16] W. C. Barrette, D. T. Sawyer, *Anal. Chem.* **1984**, *56*, 653–657, https://doi.org/10.1021/ac00268a015.
[17] Y. Nakaya, S. Furukawa, *Chem. Rev.* **2023**, *123*, 5859–5947, https://doi.org/10.1021/acs.chemrev.2c00356.
[18] S. Lu, Z. Zhuang, *J. Am. Chem. Soc.* **2017**, *139*, 5156–5163, https://doi.org/10.1021/jacs.7b00765.
[19] J. Wu, X. Gao, G. Liu, X. Qiu, Q. Xia, X. Wang, W. Zhu, T. He, Y. Zhou, K. Feng, J. Wang, H. Huang, Y. Liu, M. Shao, Z. Kang, X. Zhang, *J. Am. Chem. Soc.* **2024**, *146*, 20323–20332, https://doi.org/10.1021/jacs.4c05844.
[20] W. Ni, J. L. Meibom, N. Ul Hassan, M. Chang, Y.-C. Chu, A. Krammer, S. Sun, Y. Zheng, L. Bai, W. Ma, S. Lee, S. Jin, J. S. Luterbacher, A. Schuler, H. M. Chen, W. E. Mustain, X. Hu, *Nat. Catal.* **2023**, *6*, 773–783, https://doi.org/10.1038/s41929-023-01007-1.
[21] C. Wan, Z. Zhang, S. Wang, Q. Sun, E. Liu, H. Pu, A. Zhang, Z. Chen, A. H. Shah, X. Fu, A. N. Alexandrova, Q. Jia, Y. Huang, X. Duan, *J. Am. Chem. Soc.* **2025**, *147*, 12162–12169, https://doi.org/10.1021/jacs.5c00775.
[22] Q. Wang, Y. Cheng, H. B. Yang, C. Su, B. Liu, *Nat. Nanotechnol.* **2024**, *19*, 1442–1451, https://doi.org/10.1038/s41565-024-01716-z.
[23] H. Luo, K. Wang, F. Lin, F. Lv, J. Zhou, W. Zhang, D. Wang, W. Zhang, Q. Zhang, L. Gu, M. Luo, S. Guo, *Adv. Mater.* **2023**, *35*, 2211854, https://doi.org/10.1002/adma.202211854.
[24] Y. Li, X. Wei, R. Pan, Y. Wang, J. Luo, L. Li, L. Chen, J. Shi, *Energy Environ. Sci.* **2024**, *17*, 4205–4215, https://doi.org/10.1039/D4EE00485J.
[25] M. Li, Z. Zhao, T. Cheng, A. Fortunelli, C.-Y. Chen, R. Yu, Q. Zhang, L. Gu, B. V. Merinov, Z. Lin, E. Zhu, T. Yu, Q. Jia, J. Guo, L. Zhang, W. A. Goddard, Y. Huang, X. Duan, *Science* **2016**, *354*, 1414–1419, https://doi.org/10.1126/science.aaf9050.
[26] H. Luo, V. Y. Yukuhiro, P. S. Fernández, J. Feng, P. Thompson, R. R. Rao, R. Cai, S. Favero, S. J. Haigh,

J. R. Durrant, I. E. L. Stephens, & M.-M. Titirici, *ACS Catal.* **2022**, *12*, 14492–14506, https://doi.org/10.1021/acscatal.2c03907.
[27] R.-Z. Tai, Z.-T. Zhao, *Nucl. Sci. Tech.* **2024**, *35*, 165, https://doi.org/10.1007/s41365-024-01487-1.
[28] M. Li, K. Duanmu, C. Wan, T. Cheng, L. Zhang, S. Dai, W. Chen, Z. Zhao, P. Li, H. Fei, Y. Zhu, R. Yu, J. Luo, K. Zang, Z. Lin, M. Ding, J. Huang, H. Sun, J. Guo, X. Pan, W. A. Goddard, P. Sautet, Y. Huang, X. Duan, *Nat. Catal* **2019**, *2*, 495–503, https://doi.org/10.1038/s41929-019-0279-6.
[29] R. Y. Hodgetts, H.-L. Du, T. D. Nguyen, D. MacFarlane, A. N. Simonov, *ACS Catal.* **2022**, *12*, 5231–5246, https://doi.org/10.1021/acscatal.2c00538.
[30] X. Fu, J. B. Pedersen, Y. Zhou, M. Saccoccio, S. Li, R. Sazinas, K. Li, S. Z. Andersen, A. Xu, N. H. Deissler, J. B. V. Mygind, C. Wei, J. Kibsgaard, P. C. K. Vesborg, J. K. Norskov, I. Chorkendorff, *Science* **2023**, *379*, 707–712, https://doi.org/10.1126/science.adf4403.
[31] C. Burdis, R. Tort, A. Winiwarter, J. Rietbrock, J. Barrio, M. M. Titirici, I. E. L. Stephens, *Energy Environ. Sci.* **2025**, *18*, 5897–5901, https://doi.org/10.1039/D4EE05669H.
[32] S. Li, Y. Zhou, X. Fu, J. B. Pedersen, M. Saccoccio, S. Z. Andersen, K. Enemark-Rasmussen, P. J. Kempen, C. D. Damsgaard, A. Xu, R. Sažinas, J. B. V. Mygind, N. H. Deissler, J. Kibsgaard, P. C. K. Vesborg, J. K. Nørskov, I. Chorkendorff, *Nature* **2024**, *629*, 92–97, https://doi.org/10.1038/s41586-024-07276-5.
[33] S. Z. Andersen, M. J. Statt, V. J. Bukas, S. G. Shapel, J. B. Pedersen, K. Krempl, M. Saccoccio, D. Chakraborty, J. Kibsgaard, P. C. K. Vesborg, J. Nørskov, I. Chorkendorff, *Energy Environ. Sci.* **2020**, *13*, 4291–4300.
[34] B. Izelaar, M. Ramdin, A. Vlierboom, M. Pérez-Fortes, D. van der Slikke, A. Sajeev Kumar, W. de Jong, F. M. Mulder, R. Kortlever, *Energy Environ. Sci.* **2024**, *17*, 7983–7998, https://doi.org/10.1039/D4EE03299C.
[35] D. Jin, A. Chen, B.-L. Lin, *J. Am. Chem. Soc.* **2024**, *146*, 12320–12323, https://doi.org/10.1021/jacs.4c02754.
[36] H. F. Shurvell, M. C. Southby, *Vib. Spectrosc.* **1997**, *15*, 137–146, https://doi.org/10.1016/S0924-2031(97)00031-3.
[37] M. Spry, J. Rietbrock, O. Westhead, C. Burdis, C. Tseng, A. Morinaga, J. O. Douglas, M. S. Conroy, Y. Kondo, Y. Yamada, M. M. Titirici, I. E. L. Stephens, Y. Katayama, *Energy Environ. Sci.* **2025**, *18*, 8414–8429, https://doi.org/10.1039/d5ee01961c.
[38] B. Hammer, J. K. Nørskov, *Nature* **1995**, *376*, 238–240, https://doi.org/10.1038/376238a0.
[39] L. Zhao, Z. Z. Zhu, J. J. Wang, J. Y. Zuo, H. Y. Chen, X. Q. Qi, X. B. Niu, J. S. Chen, R. Wu, Z. D. Wei, *Angew. Chem. Int. Ed* **2025**, *64*, e202501805, https://doi.org/10.1002/anie.202501805.

Manuscript received: October 13, 2025
Revised manuscript received: December 07, 2025
Manuscript accepted: January 07, 2026
Version of record online: ■■, ■■